Materials Science & Engineering A 957 (2026) 149935

Contents lists available at ScienceDirect

Materials Science & Engineering A

journal homepage: www.elsevier.com/locate/msea

Mechanical performance during corrosion of magnesium alloy wires in artificial urine solution: Insights from an alloy study

Maria Nienaber [a,*], Mengyao Liu [b], Margarida Pacheco [d,e], Fabian Esterl [c], Merle Braatz [a], Alexandre Barros [d,e], Rui L. Reis [d,e], Mikhail L. Zheludkevich [b,f], Noomane Ben Khalifa [a,c], Sviatlana V. Lamaka [b], Jan Bohlen [a]

[a] Institute of Material and Process Design, Helmholtz-Zentrum hereon GmbH, Germany
[b] Institute of Surface Science, Helmholtz-Zentrum hereon GmbH, Germany
[c] Institute for Production Technology and Systems, Leuphana Universität Lüneburg, Germany
[d] 3B's Research Group, I3Bs – Research Institute on Biomaterials, Biodegradables and Biomimetics, University of Minho, Headquarters of the European Institute of Excellence on Tissue Engineering and Regenerative Medicine, AvePark, Zona Industrial da Gandra, Barco, 4805-017, Guimarães, Portugal
[e] ICVS/3B's-PT Government Associate Laboratory, Braga/Guimarães, Portugal
[f] Institute for Materials Science, Faculty of Engineering, Kiel University, Kiel, 24103, Germany

ARTICLE INFO

Keywords:
Wires
Magnesium
Alloy development
Extrusion
Corrosion
Artificial urine

ABSTRACT

Applications of metallic biomaterials such as sutures, knots, coils and certain types of stents require a comprehensive assessment of the resulting property profiles for the intended use case. While the feasibility of wire production and the melting and solidification behavior are a focus for additive manufacturing processing routes, mechanical properties and their development during a degradation period are of primary interest for biomedical applications. The development of distinct mechanical properties of magnesium wires can be controlled by the thermomechanical treatment applied in the manufacturing process and by the alloys used. While the conventional method for wire manufacturing involves drawing processes, direct extrusion using customized dies for enabling envisioned high degrees of deformation allows a single-stage wire production. Depending on the alloy composition different mechanical properties are achieved. This work highlights the potential for controlled development of wires for biomedical applications, demonstrating how various alloy compositions can be optimized to produce wires with the desired properties. While binary Magnesium-Yttrium maintains reasonable mechanical properties and homogeneous degradation profile also during immersion in artificial urine solution, alloys with Calcium as an alloying element revealed increasing brittleness as well as an alloy with sole Indium addition.

1. Introduction

The development of new materials for biomedical applications is a rapidly advancing field, driven by the need for biocompatible, durable, and functional materials. Magnesium (Mg) alloys have emerged as promising candidates for such applications due to their excellent biocompatibility, biodegradability, and mechanical properties [1–6]. Therefore Mg alloys have been recognized as suitable for use in medical devices such as sutures, stents, and orthopedic implants. In contemporary applications, such as surgical wire connections, it is a prerequisite that the wires can be manually formed or straightened and securely fastened by twisting or knotting which aims towards some benchmark properties of such wires [7,8]. Hence, a consistent and homogeneous mechanical property profile, along with high ductility, is envisioned, particularly during insertion and throughout service [9].

Initially, magnesium and its alloys are often considered less formable compared to other conventional materials, a perception largely attributed to their hexagonal lattice structure [10,11]. Past efforts have concentrated on the impact of alloying elements to pure Mg in general on the properties of Mg-alloys [12–14]. However, when changing the chemical composition of the respected alloy, the special impact of processing such as extrusion, rolling or drawing on microstructure and mechanical property development as a result of the thermomechanical treatment needs to be addressed as it alone also influences the respective

* Corresponding author.
E-mail address: Maria.Nienaber@hereon.de (M. Nienaber).

https://doi.org/10.1016/j.msea.2026.149935
Received 17 July 2025; Received in revised form 28 January 2026; Accepted 14 February 2026
Available online 14 February 2026

property profiles significantly [15,16]. For the special use of Mg wires for medical applications, on the one hand, the wires need enhanced formability and strength, on the other hand, corrosion/degradation properties have to be controllable for the respective applications [17–21]. It has also been noted, that beside of such alloying effects the quality of the surface may quite distinctly impact the corrosion behavior – an issue which is especially of significance for surfaces of formed materials which undergo any massive forming process or also a machining process [22,23]. In this regard it is considered that e.g. referencing the roughness of a surface is of importance, which appears to be an easily accessible property whereas other related mechanisms such as surface related strain hardening may concurrently occur.

In acknowledgement of the requirements, the present study deals with the impact of basic alloying concepts with Calcium (Ca), Yttrium (Y), and Indium (In) on both the mechanical and corrosion properties of Mg wires for an envisioned assessment against the requirements of potential degradable metallic ureteral stent applications. A combination of binary alloys (Mg-In, Mg-Y and Mg-Ca) as well as ternary alloys (Mg-In-Ca and Mg-Y-Ca) in the form of directly extruded wires with a thickness of 1 mm was therefore investigated.

Yin et al. [24] demonstrated that the corrosion behaviour of Mg-In alloys in NaCl solution can be significantly retarded due to the formation of a double-layer protective film. Furthermore, an investigation conducted by Kubásek et al. [25] in a simple simulated physiological solution (9 g/l NaCl) revealed that the degradation behaviour can be substantially reduced in a Mg-1In alloy. Deng et al. proposed a lean Mg-0.1 Ca alloy with low corrosion rate of less than 0.1 mm/y in 3.5% NaCl solution [26]. These works use cast materials for their investigations, no grain refinement due to processing has been considered. In contrast, Deng et al. [27] observed that the corrosion rate of the lean Mg-0.15Ca alloy increased significantly after heat treatment due to Fe-impurity segregation, but could be stabilized by adding indium when the alloy was in an extruded condition. In a study by Berger et al. [28], a promising solution for resorbable bone implants was developed for a lean extruded Mg-Ca alloy in ultra-high purity, which combines slow degradation, improved biocompatibility, and strong mechanical properties. For as-cast binary magnesium yttrium alloys, Liu et al. [29] demonstrated that Y retards Mg corrosion by forming a Y_2O_3 corrosion protection layer on the surface. In a previous study, Pacheco et al. [4] demonstrated the suitability of an extruded binary Mg-0.8Y wire for use in medical applications. It was also found in that work that localized corrosion occurred on occasion. In light of these findings, lowering the alloying content was envisioned. Furthermore, Ci et al. [30] have shown that the addition of trace Ca to Mg-1Y has the capacity to enhance the corrosion resistance to a significant degree. This phenomenon is primarily ascribed to the formation of a protective corrosion product film and grain refinement, which are both consequences of the addition of Ca.

Alongside the degradation properties, the formability of such related products from magnesium alloys needs attention. Numerous studies have demonstrated that yttrium alters the texture [31–33], with calcium also exerting an influence on this process [34,35]. Conversely, there is a lack of studies on indium in the extruded state. A variety of methods exist for the manufacture of magnesium wire; however, the most common technique for producing thin wires involves the application of drawing processes of extruded rods [36,37]. In contrast, direct extrusion is a method that has the potential to produce wires in only one process step with a high extrusion ratio [38–40].

The objective of this research is to understand how different alloy compositions affect the microstructure, texture, degradation, and mechanical properties of Mg alloy wires and contribute to a broader understanding of alloying effects on such properties.

2. Material and methods

Five magnesium alloys were considered in this study and were available in the form of cast ingots. The chemical compositions of these alloys were measured by using X-ray micro fluorescence (M4 Tornado, Bruker), and the results are collected in Table 1. The billets were machined to a length of 75 mm and a diameter of 49 mm for extrusion of wires with a 1 mm diameter. A solid solution heat treatment was carried out for 16 h at 400 °C, followed by air cooling. The appropriate temperature for this heat treatment has been revealed based on thermodynamic data in the form of quasi-binary phase diagrams from PANDAT 2018 database. Direct extrusion of wires was achieved by conventional extrusion, using an automatic 2.5 MN extrusion press (Müller Engineering GmbH & Co. KG, Todtenweis/Sand, Germany). The billets were preheated for 60 min to the extrusion temperature of 400 °C in an air-circulating furnace (Nabertherm). The die employed for the extrusion experiments comprised four nozzles with a round shape and an identical diameter of 1 mm. This refers to an extrusion ratio of 625 and a degree of deformation of 6.4, correspondingly. Thus, four wires were extruded concurrently, and an automatic coiler system was utilized to coil the wires. The details of the setup and the experimental scheme have also been presented in an earlier work [38].

A confocal laser-scanning microscope VK-1000 (Keyence) was used for an optical surface characterization of the wires in the as-extruded state in differential interference contrast (DIC) and after deformation. To define the surface roughness, the arithmetic mean height S_a was derived from the evaluation as the area-related value of the deviation of the surface height from its arithmetic mean value. The low-pass filter was set to 0.8 μm, and the high-pass filter to 0.05 mm. Surface measurements were conducted on three separate areas to obtain a mean value and its standard deviation. Microstructure and texture analysis of the wires in different conditions were carried out using electron backscatter diffraction (EBSD) measurements with a field emission scanning electron microscope (SEM) Zeiss Ultra equipped with an EDAX-TSL OIM system. An acceleration voltage of 15 kV was used and the measurements were carried out with a step size of 0.5 μm for the as-extruded wires and 1 μm for the wrapped wires. High-angle grain boundaries (HAGB, with misorientation angles larger than 15°) are marked in black. Furthermore, for the wrapped wires, a Kernal Average Misorientation (KAM) analysis was conducted to quantify the extent of deformation. KAM is a point property referring to the average misorientation between neighboring measuring points. The use of a color scale enables the presentation of the average misorientation in relation to a defined group of the second neighbor points. The structure exhibits a low misorientation, indicated by a blue color scale value of 0°, and a high misorientation, indicated by a red color scale value of 5°. In addition, the inverse pole figures (IPF) are shown. Sample preparation was based on conventional metallographic procedures such as grinding (#1200, #2500 and #4000) and polishing with oxide polishing suspension. Additional electro-polishing was carried out using Struers AC2 solution cooled to −10 °C for 20 s at a voltage of 22 V.

The mechanical properties of the wires were revealed from tensile tests using a 5 kN universal testing machine of Zwick at ambient temperature. A gauge length of 40 mm and an initial strain rate of 10^{-3} 1/s were kept constant for the experiments. The strain was directly measured via an extensometer. For referring to a more application related perspective of the mechanical behavior, knot forming and wrapping of spirals have been considered. The methods relate to procedures in bone surgery, therefore a simple „knot test"is adopted to analyze the ability of the wire to withstand non-uniaxial straining [21]. For this, a knot is formed manually with a diameter of 7 mm. The ends of the wire are clamped into the above-mentioned testing machine, and stress is applied using a strain rate of 10^{-2} 1/s until the fracture of the sample, which occurs in the vicinity of the knot. The ratio of the fracture stress to the ultimate tensile stress (UTS) is a stress ratio used to analyze the ability of the material to maintain its ductility in this more complex forming configuration. Wrapping tests were carried out manually in accordance with ISO 7802: 2013 at room temperature with a defined inner diameter of 1.5 mm and at least 6 windings were wrapped. Note,

Table 1
Chemical composition in wt% (Mg in balance).

Mg-Alloy	Ca	In	Y	Fe	Cu	Al	Si	Mn
X0	**0.15**	-	-	0.0049	0.0006	0.0056	0.0146	0.0268
I1	0.0046	**0.61**	-	0.0042	0.0004	0.0070	0.0151	0.0260
W0	0.0076	-	**0.34**	0.0048	0.0008	0.0092	0.0072	0.0263
IX10	**0.15**	**0.61**	-	0.0050	0.0006	0.0042	0.0162	0.0264
WX00	**0.15**	-	**0.35**	0.0035	0.0006	0.0186	0.0076	0.0257

that spirals relate to an envisioned shape of a stent application for the ureteral track, see indication in earlier work [4].

Five pieces of the original as-extruded wire of each composition with a sample length of 11-12 cm were used for immersion tests in an artificial urine solution (AUS). The detailed composition of artificial urine is listed in Table 2 [41]. The initial pH of the AUS was adjusted to 7.0 ± 0.2 by addition of dilute NaOH solution. All samples were immersed at 37 °C for 14 days. Only the wires of alloy I1 were immersed for 7 days due to its faster corrosion. 0.5% Penicillin-Streptomycin [42,43] (Gibco, 10000 units/mL Penicillin (1 unit penicillin = 0.6 μg), 10000 μg/mL Streptomycin) was added to the AUS for avoiding bacterial contamination. The flow rate was 0.5 mL min^{-1}. The total initial volume of the corrosive solution was 5 L. It was continuously renewed by the fresh AUS, by displacing the old solution with the new solution at the rate of 0.5 mL min^{-1}. After immersion, the corrosion products were removed by the chromic acid solution (200 g/L CrO_3). The corrosion rate was calculated by the following formulas [44]:

$$CR_{wt} = \frac{W_0 - W_t}{A \cdot t} \tag{1}$$

where CR_{wt} is the corrosion rate (mg·cm^{-2}·h^{-1}); W_0 and W_t are the weight before and after immersion (mg), A is the test area of the sample (cm^2) and t is the test period (h). Error bars are the standard deviation of independent samples (n = 5). The corresponding corrosion rate P_w (mm·y^{-1}) is obtained by Eq. (2) [45]:

$$P_w = 50.4\ CR_{wt} \tag{2}$$

Optical micrographs of the wires after immersion in AUS were acquired using Sony Alpha 7R camera. Electron micrographs were taken by using scanning electron microscopy with a Tescan VEGA at accelerating voltage of 15 kV, and current 30 pA in secondary electron detection mode. After removing the corrosion products, the surface of metallic samples was conductive, no carbon/gold was deposited.

3. Results and discussion

Basic processing results from the wire extrusion experiments are collected in Table 3. Although the process parameter settings were not initially changed, resulting exit speeds varied for the different alloys due to the distinct flow behavior in this high degree of deformation environment. Variations occur in the extrusion exit speed and the extrusion force, contingent on the alloy composition. The occurrence of a peak force marks the initiation of material flow, whereby the force level itself depends on the alloy-specific flow stress of the material in its particular condition. Additionally, a force component is included, which refers to the friction between the billet and the container wall. Given that all billets have the same initial length, the friction component is assumed to be comparable. For the binary alloys, pure Y in alloy W0 marks the highest peak force level and therefore the highest increase in flow stress, followed by Ca in alloy X0. The pure alloying with In in alloy I1 reveals the lowest peak force. In combination with Ca in the alloys IX10 and WX00 this likewise increases the peak force level. With respect to the extraordinarily high degree of deformation, none of the alloys reaches the maximum capacity of the extrusion press at 2.5 MN, and as the coiling of wires has been shown feasible throughout, the processability of the alloys is confirmed.

Table 2
Composition of Artificial Urine Solution, according to Ref. [41]. Additionally, Gibco Pen Strep was added and the initial pH was adjusted to 7.0 ± 0.2.

	Molarity (mM)	Quantity (g/100 ml)
Na2SO4	11.965	0.17
C5H4N4O3 (Uric acid)	1.487	0.025
Na3C6H5O7·2H2O (Na citrate dihydrate)	2.45	0.072
C4H7N3O (Creatinine)	7.791	0.0881
CH4N2O (Urea)	249.75	1.5
KCl	30.953	0.2308
NaCl	30.053	0.1756
CaCl2	1.663	0.0185
NH4Cl	23.667	0.1266
K2C2O4.H2O (K oxalate)	0.19	0.0035
MgSO4·7H2O	4.389	0.1082
NaH2PO4·2H2O	18.667	0.2912
Na2HPO4·2H2O	4.667	0.0831

Table 3
Experimental data from wire extrusion and estimated exit temperature.

Alloy	Wire exit speed [m/min]	Peak force [MN]	Estimated temperature range [°C]
X0	**6.4**	**1.56**	**423–426**
I1	**5.4**	**1.05**	**418–421**
W0	**3.6**	**1.81**	**412–413**
IX10	**6.4**	**1.72**	**423–426**
WX00	**3.9**	**1.86**	**412–413**

All tests were conducted at an extrusion temperature of 400 °C. Still, it has been shown that a variation of extrusion speeds in the forming zone may impact the resulting property profiles of the extrudates [35]. To gain general insights into the temperature development based on varying wire exit speeds, the exit temperature was determined and compared using finite element analysis for the above-described extrusion setup (see Fig. 1). The numerical model was set up in commercial simulation software *QForm Extrusion* 11.1.0, employing Arbitrary Lagrangian-Euler formulation. Here, the model was discretized using three-dimensional tetrahedra as building blocks. Overall, the model consists of 1,008,758 volumetric elements with 186,531 nodes in total. Further, the temperature calculation was discretized in the finest available setting. The material model used for the extrusion tools is sourced from the built-in material library. As for the billet material, the simulations were carried out for two different alloys, namely AZ31 and ZX10, instead of the experimental alloy selections of this study. The material models used for these alloys have previously been validated as published in Esterl et al. [46]. Additionally, the friction between the billet and the tools was incorporated by applying Levanov's friction law [47], given by:

$$\tau_F = m\, \frac{\sigma_F}{\sqrt{3}} \left(1 - \exp\left(-L\, \frac{\sigma_N}{\sigma_F}\right)\right) \tag{3}$$

Here, the friction stress τ_F is calculated based on the flow stress of the workpiece material σ_F, the normal contact pressure σ_N, the friction factor m and the Levanov coefficient L set to be 1 and 1.25, respectively, following their default values. For the validation of the numerical setup,

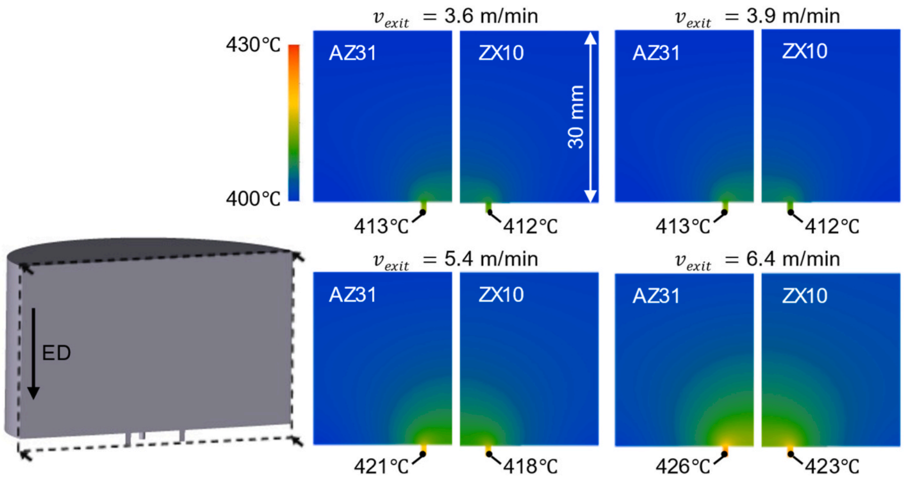

Fig. 1. Simulated temperature evolution in the cross section of the billet based on varying exit velocities after a ram displacement of about 45 mm for AZ31 (left) and ZX10 (right).

previously published experimental data has been used and the simulated billet length and exit velocities have been adapted accordingly [48]. Therefore, comparing the maximum extrusion load for the numerical setup with the experimentally obtained maximum extrusion load, the absolute difference is only about 8 % for AZ31 and 12 % for ZX10. Based on varying exit speeds measured in this study, the differences in temperature evolution for AZ31 and ZX10 are within the range of only 13 °C, see Fig. 1. As a comparable temperature range is estimated for the alloys investigated within this study, it is hypothesized that potential differences in the temperature evolution will not dominate the resulting microstructure development of the wires.

As illustrated in Fig. 2, the surfaces of the extruded wires in this study exhibit notable variations. Despite utilizing identical extruding parameters, the wires possess distinct surface characteristics, visible in the LSM images, corresponding surface line scans and the surface roughness as the arithmetic mean height (S_a). The W0 wire demonstrates the most uniform surface characteristics, as evidenced by minimal deflections in both the vertical and horizontal line scans, as well as the lowest surface roughness value with 0.26 μm. In comparison, the IX10 and WX00 alloy wires exhibited a surface that was slightly more uneven than that of the W0 wire (Sa: 0.37 μm respectively 0.50 μm). The X0 wire shows a uniformly rough surface, while the I1 wire exhibits a significantly rougher surface, showing an extremely uneven wavy surface as evident especially in the horizontal line scan along the wire direction. Also in the surface roughness the I1 wire has the highest value with 0.71 μm. This already reveals the influence of the alloy composition on the extrudability and the influence on the surface. In this case the extraordinary difference is marked by the rough surface of I1 alloy.

Fig. 3 collects corresponding SEM images in combination with EDX measurement (marked by arrows and the matrix measurements (M) by lines around the measurement areas) to reveal the chemical composition of the matrix and second-phase particles. Compositions of the analyzed points or areas are collected in Table 4. The applied solution annealing of the billets at 450 °C and the selected high extrusion temperature of

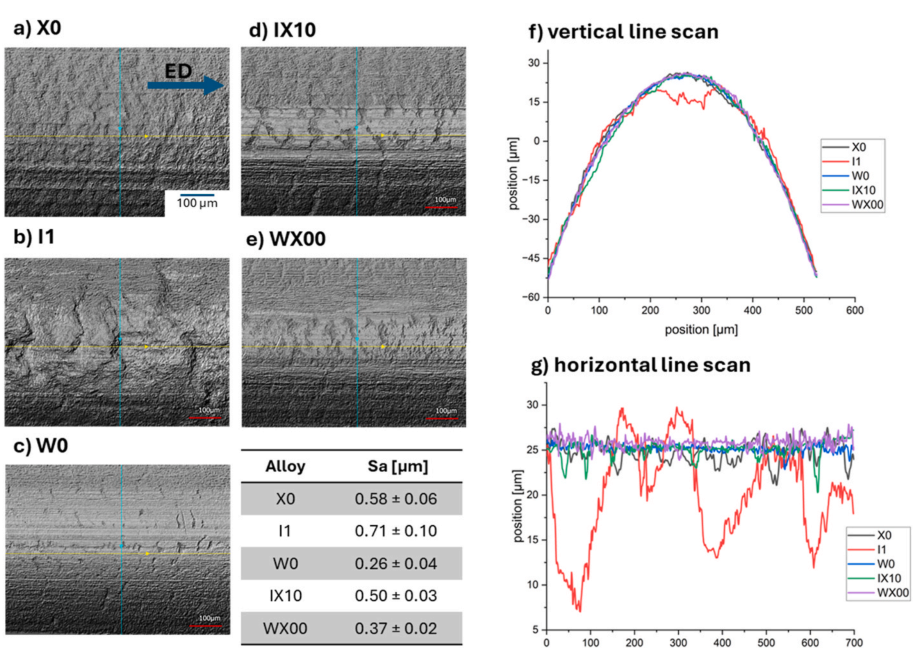

Alloy	Sa [μm]
X0	0.58 ± 0.06
I1	0.71 ± 0.10
W0	0.26 ± 0.04
IX10	0.50 ± 0.03
WX00	0.37 ± 0.02

Fig. 2. Surface characterization of the as extruded wires with the average surface roughness (Sa): a-e) LSM images of the wires in DIC contrast; Line scans f) vertical and g) horizontal.

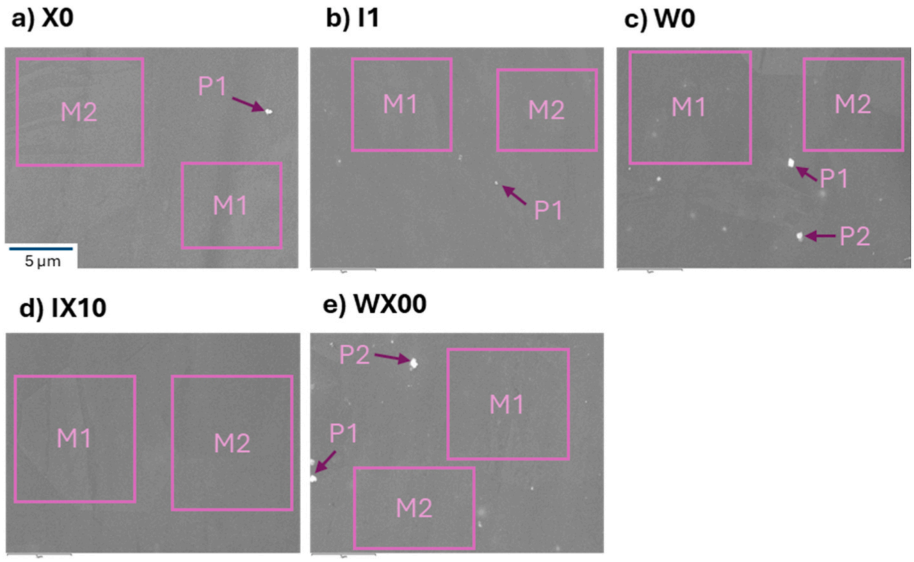

Fig. 3. Scanning electron microscope (SEM)-Image in 10000 × magnification with locations of the EDX scans of the extruded wires (extrusion direction (ED) vertical).

Table 4
Chemical analysis of the highlighted areas in Fig. 3 (Mg in balance).

Alloy	in wt%	Ca	In	Y	Cu	Fe	Mn
X0	M1	0.14	-	-	-	-	-
	M2	0.11	-	-	-	-	-
	P1	0.11	-	-	1.78	-	-
I1	M1	-	0.53	-	-	-	-
	M2	-	0.51	-	-	-	-
	P1	-	0.41	-	-	3.09	0.26
W0	M1	-	-	0.24	-	-	-
	M2	-	-	0.25	-	-	-
	P1	-	-	19.41	-	0.11	-
	P2	-	-	11.39	-	-	-
IX10	M1	0.11	0.43	-	-	-	-
	M2	0.13	0.53	-	-	-	-
WX00	M1	0.23	-	0.35	-	-	-
	M2	0.16	-	0.23	-	-	-
	P1	0.59	-	18.94	-	0.1	-
	P2	0.57	-	14.96	-	-	-

400 °C aimed to maintain all alloying elements in solid solution and to not enable precipitation of second phases. However, in W0 (P1, P2) and WX00 (P1, P2), particles are found in the microstructure which exhibit a notably high proportion of yttrium, ranging from 11 to 19 wt%. This is consistent with earlier findings in Mg-Y-alloys [49], where such particles are likely identified as thermally stable Y-hydrides. Other particles can be attributed to impurity inclusions. X0 exhibits a Cu containing particle P1, whereas this element is not an intended part of the alloy composition, while in I1 a particle P1 includes Fe and Mn. The matrix (M) related area measurements by using EDX revealed only slight deviations from the chemical analysis indicated in Table 1. The Ca-containing alloys have a Ca content of 0.11-0.14 wt%, the indium content varies between 0.41 and 0.53 wt%, and the yttrium between 0.24 and 0.35 wt%.

The grain structures and corresponding textures of the wires measured from longitudinal sections by EBSD are shown in Fig. 4. High-angle grain boundaries (HAGB, with misorientation angles larger than 15°) are marked in black. The corresponding average grain sizes are added into the orientation maps. All wires reveal a completely recrystallized microstructure with equiaxed grains. The I1 wire has by far the coarsest grain structure with an average grain size of 30 µm. Some visible twins in the microstructure are the remains from sample preparation, which is sometimes hard to avoid especially in large grains and in wires which ease local deformation during sample preparation. The homogenous recrystallized microstructures exhibited only disparities in terms of the mean grain size of the respective alloy wires.

The other alloys are much finer grained and the differences among them are only small with average grain sizes between 8 and 13 µm. As the forming procedure as well as the processing parameters have been kept constant, the above mentioned impact of varying extrusion speeds may impact the microstructure development besides the impact of the alloying elements themselves. If small changes in the significance of recrystallization and grain growth occur due to a rate impact of the acting forming temperature inside the die during extrusion, I0, X0 and IX10 compare well with similar exit speeds, whereas IX10 exhibits a slightly finer grained microstructure compared to X0. Thus, besides the fact that grain growth is not anyhow retarded in the binary I0 alloy, a very slight – if any-higher ability to grain growth may be visible due to the addition of In to the X0 alloy in IX10. Likewise, only the Y-containing alloys W0 and WX00 seem to be restricted to a lower extrusion speed, potentially resulting in slightly lower forming temperature of both alloys. While such an effect can meet the lowest achieved extrusion speed of alloy W0, it does not change distinctly with the addition of Ca into alloy WX00 which exhibits a coarser microstructure within the small range of grain sizes compared to W0 without Ca. In summary, Indium as a sole alloying element does not emphasize a distinct grain refinement during dynamic recrystallization, Ca and Y do so as sole alloying elements where Y seems to exhibit a higher propensity to such grain refinement. While Ca maintains this role in ternary IX10, it does not add up this tendency in WX00 which remains coarser grained.

The inverse pole figures in the extrusion direction (ED) are also shown in Fig. 4 to represent the full texture of the wires. The presence of a distinct <10-10> fibre texture in alloy I1 is indicative of the typical outcome of symmetrical extrusions of magnesium alloys [50,51]. This particular texture is known to impede the enhancement of ductility or formability of the materials. The addition of Ca into IX10 appears to weaken this distinctive component, thereby establishing a so-called "rare earth texture" of such magnesium alloys, characterized by a broader angular distribution of basal planes and a distinct tilt of basal planes out of the dominant extrusion direction [52–54]. It is interesting to note that a very similar texture is obtained for X0 as well as a stronger version for W0. However, in the case of WX00, no clear alignment of basal planes parallel to the extrusion direction is found anymore. In comparison to previous studies [52,55], where such alterations in texture are more readily apparent, the present investigation must consider the extremely high degree of deformation, which may result in

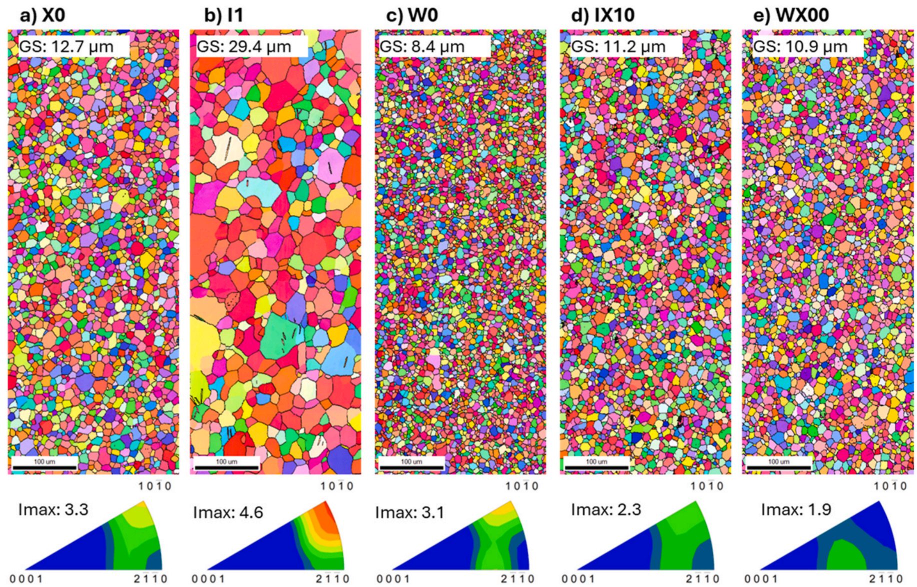

Fig. 4. Orientation maps from EBSD measurements on longitudinal section of the as extruded wires (extrusion direction (ED) vertical) and the corresponding inverse pole figures in the extrusion direction (ED).

the predominant deformation texture (i.e. the <10-10> fibre component) remaining more robust during the process of recrystallization. In summary, WX00 is the only alloy of this study which reveals a typical texture with full tilt of basal planes whereas IX10 as well as X0 and W0 show a transitional double-fibre of <10-10> and the tilt component. This finding meets earlier elaborations along with the extrusion of magnesium alloys, where such texture weakening has been used to increase ductility of extrudates as well as isotropy between tensile and compressive deformation. This has been based on various effects of balanced recrystallization mechanisms of dynamic recrystallization mechanisms [52–54] and has been associated with the alloying with RE elements or Ca in the past.

None of the AUSs reported so far, including those listed in the "Standard Specification for Ureteral Stents" F 1828– 97 (2006) [56], was specifically designed to study metals' degradation. Thus, compounds that significantly affect the degradation of metals might be encountered in AUSs currently in use. For example, AUS containing sodium sulfite is obviously not suitable for testing metallic materials, as oxygen reduction reaction is the dominant cathodic process for Zn- and Fe-alloys [57,58] and an important secondary cathodic pathway for Mg alloys [59,60]. Being a strong oxygen scavenger, sulfite depletes oxygen concentration in AUS, significantly inhibiting cathodic reaction and the entire degradation process [17]. In the absence of standard AUS suitable for testing metallic materials, we choose to experiment with the AUS proposed by Sarigul et al. [41], as their AUS composition mimics urine of healthy individuals (as far as a single composition can mimic large variation ranges of multiple urine components characteristic even of healthy individuals). Additionally, penicillin-streptomycin mixture was added to minimize the microbial growth (the function that otherwise would be largely performed by oxygen scavenger, sodium sulfite) and the initial pH was adjusted to 7.0 ± 0.2 as pH an important factor influencing the corrosion rate of magnesium.

The weight loss results and corresponding corrosion rates of the alloy wires are collected in Fig. 5. Four out of five alloys were immersed for 14 days. The exposure of alloy I1 wires was stopped after 7 days, as it revealed the highest corrosion rate among the five tested alloys. The other four alloys, including the Ca-modified Indium-containing alloy IX10 were exposed for full 14 days in AUS and exhibit rather low similar corrosion rates well below 0.2 mm/y. It has been previously reported that Mg-Ca alloys show a tendency of increased corrosion rate due to thermal processing such as hot extrusion and concurrent annealing such

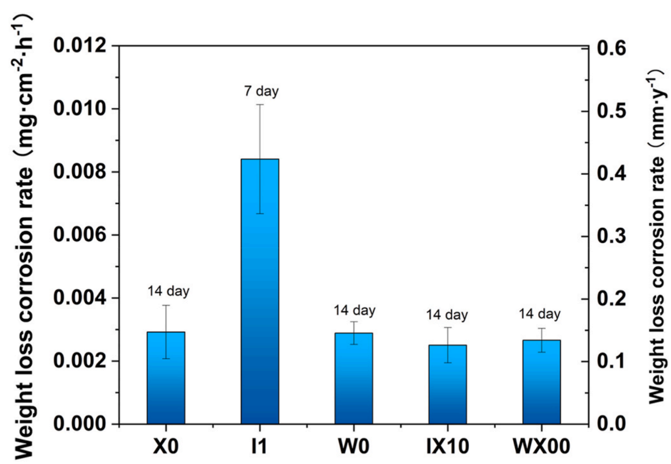

Fig. 5. Corrosion rate of different Mg alloy wires calculated based on gravimetric weight loss after full immersion in artificial urine solution.

alloys. This effect has been previously explained by a promotion of Fe-precipitation in the underlying thermal driven process [27]. While In as a sole alloying element increased corrosion rate, alloying the Mg-Ca with In allows alleviating formation of Fe-rich precipitates. Thus, slightly lower corrosion rate of IX10 compared to X0 is fully in line with our previous report [27]. W0 (Mg-Y) demonstrates corrosion rate similar to that of IX10 and X0, same as alloying Mg-Y with low amount of Ca (WX00), does not increase corrosion rate either.

Fig. 6 shows the visual appearance of five wire types after exposure to AUS for 7 (I1) or 14 days (all other wires). Pitting-like deep defects, characteristic to I1 and less so to X0, are pointed out by the blue arrows. No events of strongly localized corrosion were found in three triplicates of IX10, WX00 and W0 wires. Apart from these single events of localized corrosion, which are critically detrimental for long ureteral stents, relatively even degradation was evidenced by closer examination by SEM.

Stress-strain diagrams from tensile tests of the wires in the as-extruded condition are shown in Fig. 7a. While the impact of corrosion in artificial urine solution is described later, Fig. 7b also collects the mechanical behavior of the same wires after corrosion in AUS for the

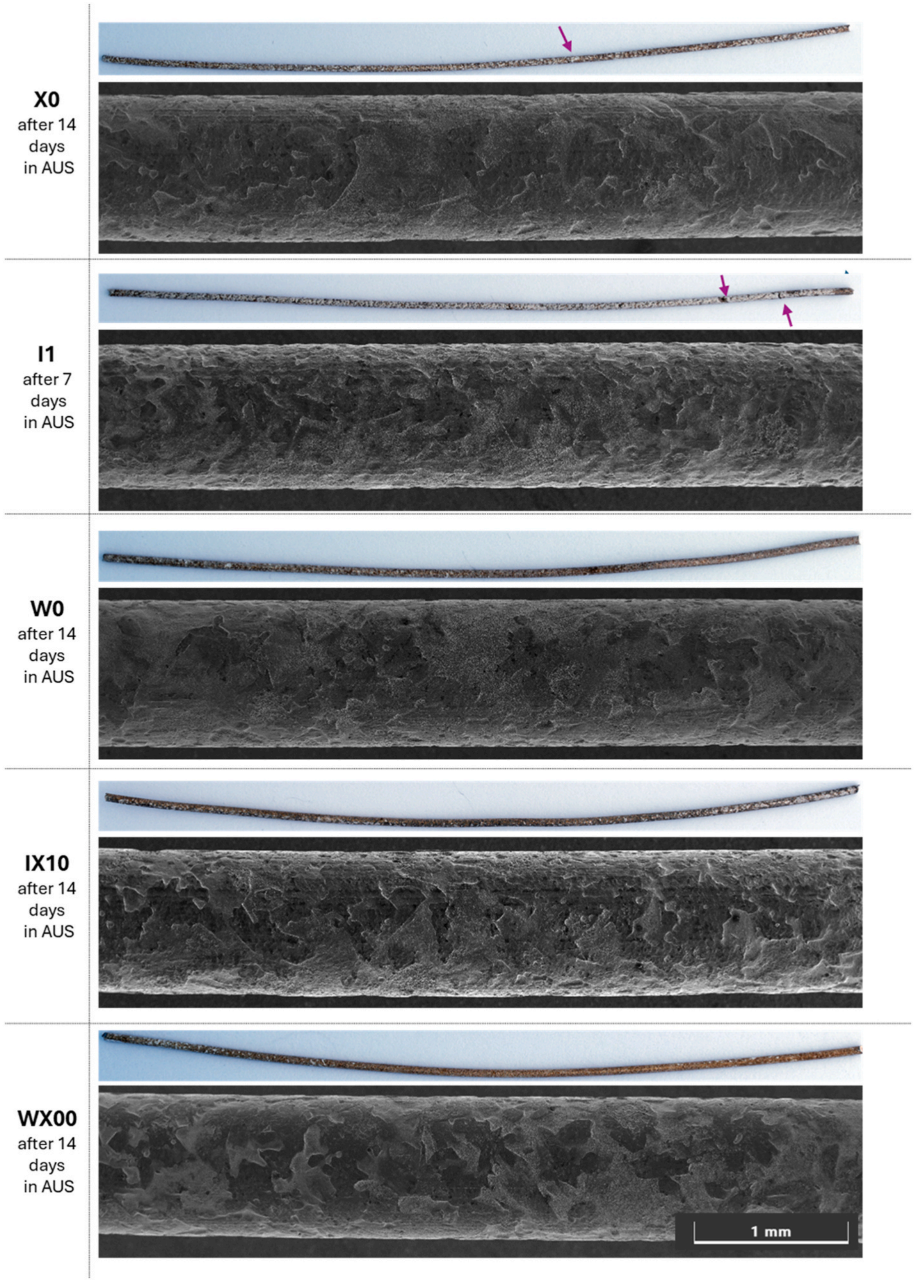

Fig. 6. Optical photographs (upper) and SEM micrographs of five wire types, after immersion in AUS and removing corrosion products with chromic acid. The initial diameter of each wire was 1 mm. The arrows in the optical micrographs point to the deep, pitting-like defects, representative of I1 and X0 corrosion profile.

comparison of the original alloy behavior with respect to the development of the microstructure during forming as well as the impact of the corrosive environment in AUS solution. Table 5 collects the mechanical properties of all tested wires. In the as-extruded condition, only alloy I1 exhibits clearly limited ductility with a fracture strain of 4.6% as a result of brittle failure of the wire. Further, also the stress properties TYS and UTS remain comparably low, especially if it is considered, that the underlying strong fibre texture requires higher stresses for activation of basal slip compared to materials with weaker textures. This can directly be regarded to the coarse-grained microstructure of the material and the distinct alignment of basal planes as a result of the strong texture.

The other alloy wires all exhibit a more advantageous mechanical performance with higher uniform strain and fracture strain. The highest strain levels are received from alloy WX00. It's straining behavior is associated with a certain S-shaped curve, alongside with the weakest texture and most distinct off-basal character of the wire. This also explains the lowest TYS of all wires of this study, still maintaining the highest ability to strain hardening if measured as the difference between UTS and TYS. The other wires reveal higher TYS and UTS where the finest-grained alloy W0 also exhibits the highest values. X0 reveals the lowest fracture strain in tension (excluded I1) among these other alloys W0, IX10 and WX00 with an intermediate texture maintaining the <10-10> fibre component to some degree.

After an immersion of the wires in AUS, the representation of mechanical properties changes distinctly (Fig. 7b), especially with respect to the fracture behavior, which remains brittle at very low levels of strain. Only for W0 is the original level of ductility maintained in the applied tensile stress environment. The impact of the corrosion on fracture strain is dramatic for all other alloys, with the stress levels not changed significantly. The drop in the case of I1 appears not extremely significant, however, the original fracture strain was already very low. Note that the Ca-containing alloys all exhibit this drop in ductility after

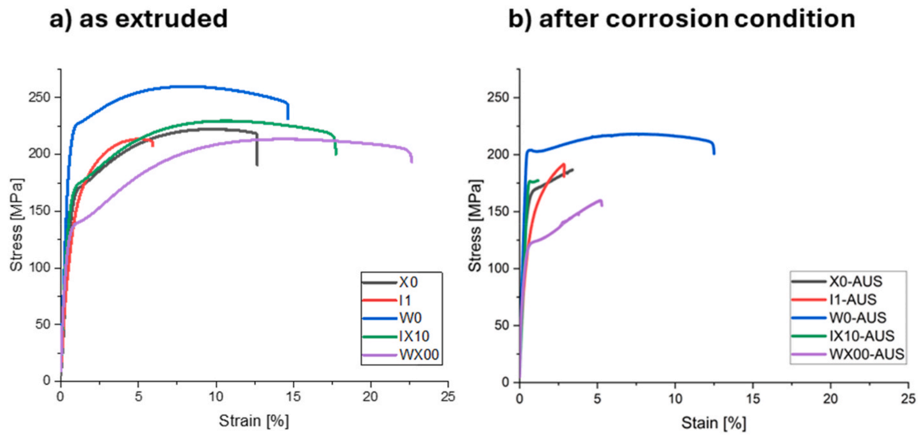

Fig. 7. Representative stress–strain diagram in ED from the wires in a) as extruded and b) after corrosion condition, n = 3 (example curves in Fig. 7b refer to those with highest achieved strain).

Table 5
Mechanical properties from tensile tests parallel to ED (tensile yield stress (TYS), ultimate tensile stress (UTS)) with standard deviations and grain size calculated from the EBSD measurement (Fig. 3).

Alloy	Condition	TYS [MPa]	UTS [MPa]	Uniform strain [%]	Fracture strain [%]	Grain size [μm]
X0	AE	153 ± 1	222 ± 1	8.7 ± 0.3	11.8 ± 0.3	13 ± 2
	AUS	150 ± 5	171 ± 16	3.1 ± 1.3	3.1 ± 1.3	
I1	AE	167 ± 2	214 ± 3	3.5 ± 0.1	4.6 ± 0.2	29 ± 5
	AUS	126 ± 4	163 ± 29	2.7 ± 1.8	2.7 ± 1.8	
W0	AE	210 ± 4	256 ± 4	**7.6 ± 0.3**	**13.7 ± 0.5**	8 ± 2
	AUS	197 ± 7	202 ± 5	**7.2 ± 0.2**	**10.9 ± 0.4**	
IX10	AE	154 ± 1	225 ± 4	9.8 ± 0.2	17.1 ± 1.1	11 ± 3
	AUS	165 ± 8	173 ± 3	1.1 ± 0.1	1.1 ± 0.1	
WX00	AE	129 ± 3	209 ± 5	13.4 ± 0.1	21.4 ± 0.7	11 ± 2
	AUS	112 ± 2	151 ± 9	4.2 ± 1.4	4.2 ± 1.4	

immersion in the AUS solution. While TYS remains mostly not much affected, the stress levels up to UTS are often lower compared to the non-corroded samples, hypothetically due to unrevealed local changes of the accounted cross section due to localized corrosion. Lower levels for UTS are consistent with the lower fracture stresses and the inability of the materials to reach maximum strain hardening before a brittle fracture occurs. This also correlates with the degradation rate as shown in Fig. 5.

Fig. 8 collects images of the wires after the knot test and a table which includes the corresponding stress ratios in the form of the ratio between the fracture stress during the knot test and the UTS taken from quasistatic testing (Table 3) and the local surface roughness as mean arithmetic height (S_a). In Fig. 8f, the technical set up and the form of sample are shown. Starting with X0, it was found that this wire could still be knotted, but there was a deep crack in the forming zone and the entire surface developed a rather rough structure. The I1 wire was the only wire that could not be completely knotted, a finding which is also clearly reflected in the lowest stress ratio. This correlates with the strongest texture and the lowest ductility among the wires of this study. The W0 wire exhibited a less pronounced development of the surface structure following the knot test and demonstrated a marginally higher stress ratio. A comparison of the ternary alloys with the binary alloys revealed higher stress ratios in both cases IX10 and WX00, respectively. Additionally, both wires demonstrated a more compact knot structure. The surface development clearly depends on the alloy but does not follow a potential sequence of grain size as indicated in Table 3. Roughness measurements (including in Fig. 8) reveal the least developing change for WX00, whereas X0 and especially I1 show a distinct increase. Note that I1 originally also has been the material with the most distinct surface structure as a result of the extrusion of the wires itself. The sequence of surface structure development corresponds with the original ductility of the alloys and the corresponding texture, leaving WX00 with highest strain levels as well as the weakest texture, the smoothest of the wires and vice versa I1 the roughest.

In addition to the knot test, also wrapping tests were carried out around a diameter of 1.5 mm (Fig. 9) which allows receiving insight into the behavior of the alloys following stress conditions close to the envisioned demonstrator of a ureteral stent shape [61,62]. Both I1 and X0 broke during the first wrapping, which excludes them from the presentation in Fig. 8 as feasibility could not be shown. This material failure can be linked to the behavior of the wires during the knot test as well as the ductility of the material. As previously demonstrated, I1 and X0 have the lowest ductility and strongest <10-10>-fibre component of the textures, which are unfavorable for enhanced formability of the wires. This correlates with a reduced biaxial forming ability. As illustrated in Fig. 9a, the wires W0, IX10 and WX00 were successfully wound around a diameter of 1.5 mm. Furthermore, a detailed analysis of the forming behavior was conducted on these wires using local EBSD measurements on longitudinal sections of the formed wires (as shown in the figure). In Fig. 9b, measurements are displayed with different highlighted orientation fractions as labelled in the respective legend of the corresponding (0001) pole figure of basal plane orientations. The orange and red fractions correspond to basal planes aligned parallel to the extrusion direction, with the c-axis positioned either vertically or horizontally relative to the measured mid-plane, respectively. The variation of grain orientations is typically associated with the round shape of the wire itself. This orientation dominates the texture on the right side of the images which refers to the outer surface of the respective wires, thus describes this aspect of the microstructure in a tensile strained range of the biaxial forming procedure of wrapping grains with basal orientation titled by approximal 90° to the extrusion direction are labelled in green. These grain orientations do not stem from the original wire texture but mark a change in the local orientation distribution at the inner part of

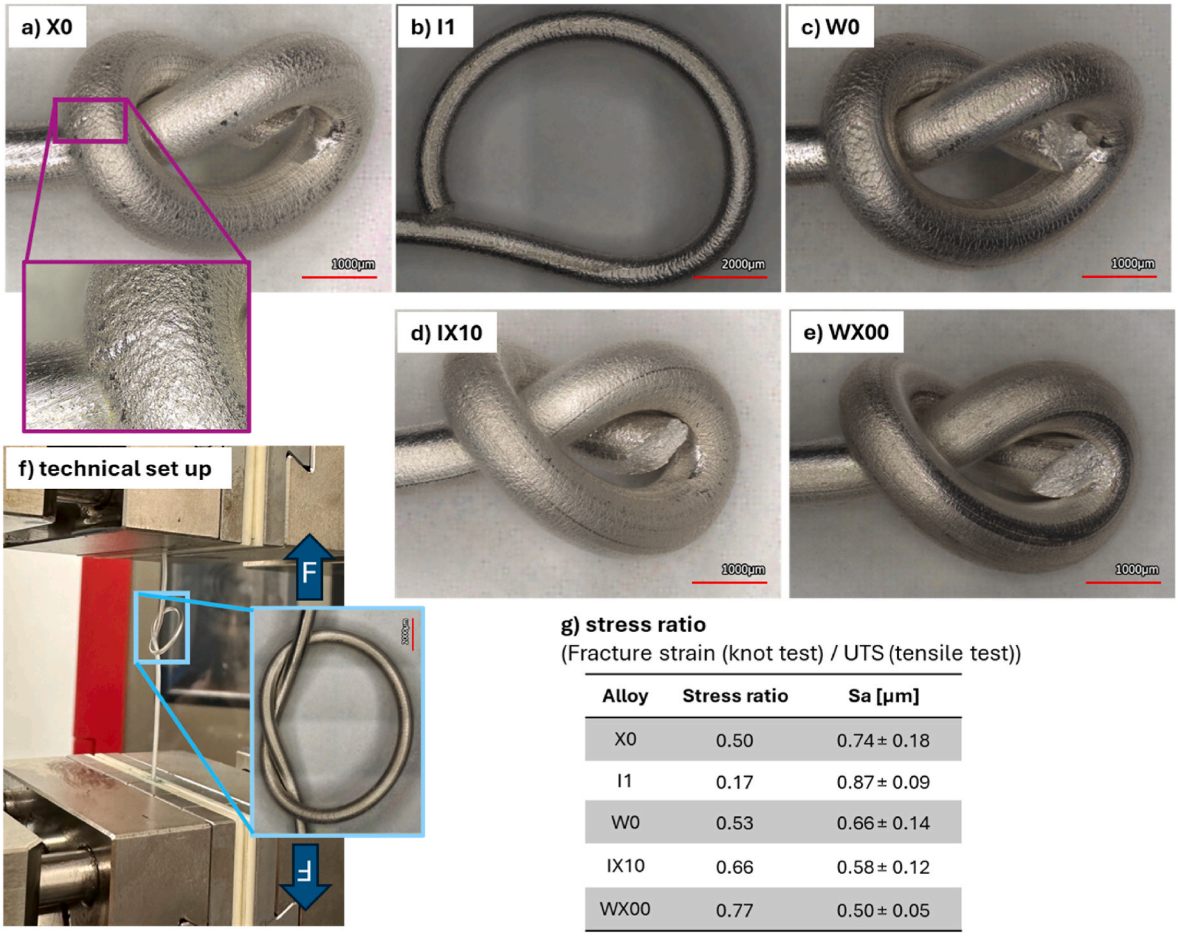

g) stress ratio
(Fracture strain (knot test) / UTS (tensile test))

Alloy	Stress ratio	Sa [μm]
X0	0.50	0.74 ± 0.18
I1	0.17	0.87 ± 0.09
W0	0.53	0.66 ± 0.14
IX10	0.66	0.58 ± 0.12
WX00	0.77	0.50 ± 0.05

Fig. 8. Optical images of the wires after the knot test with the corresponding stress ratios and the local surface roughness.

the wire which in tendency experienced compressive strain in relation to the extrusion direction as a result of bending. It becomes evident that this affects only a small range of grains along the through-thickness measurement.

However, it can also be seen that the different areas are pronounced to varying degrees depending on the alloys. Under tensile strain, a prismatic plane alignment typically forms, resulting in higher intensity for the <1010> pole, which also describes the change in grain structure [63,64]. In the green area (left), i.e. the inner part of the bend wire where compressive stress mainly acts on the grains, a complete tilt of the basal planes and the corresponding c-axis parallel to the ED can be observed, indicating that this part of the microstructure undergoes twinning. Note that the alloy with the least district difference of the change in the orientation distribution is WX00 which is the one with the weakest texture of the original wire without visible <10-10> prismatic fibre component. The grains also appear flattened horizontally, i.e. perpendicular to the wire extrusion direction. A consideration of KAM measurements (Fig. 9c), i.e. the strain distribution in the material as measured from local point-to-point misorientations, reveals discrepancies with respect to the position and for the three alloys. The structure exhibits low misorientation, indicated by a blue scale value of 0°, and high misorientation, indicated by a red scale value of 5°. Red areas are deformed, while green/blue areas are not subjected to deformation. On the one hand, the transition from compressive to tensile stress can be clearly delineated by a neutral phase, and a texture analysis of the neutral phase, Fig. 9d, revealed no significant difference from the initial texture, indicating that no deformation mechanisms were active here. On the other hand, depending on the alloy, WX00 and IX10 exhibit the broadest neutral phase, while W0 shows the highest fraction of red areas in the KAM analysis, indicating deformation. This observation is further corroborated by the results of the knot test, which demonstrate that WX00 and IX10 exhibit superiority in terms of their ability to absorb stresses. This enhanced capacity is attributable to the high ductility of the material, as evidenced by the texture analysis.

4. Conclusion

Extrusion of Mg alloy wires with diameter of 1 mm has been shown feasible at high degrees of deformation. The resulting microstructures are similar compared to typical round bar extrusions of magnesium alloys while favoring a stronger pronunciation of a prismatic fibre component which limits strain properties of the materials. Only a combination of Y and Ca in alloy WX00 can overcome the stabilization of this deformation related texture, revealing the lowest TYS and UTS but the highest strain properties of this alloy. A sole stabilization of properties in a binary Mg-In alloy I1 was not found with the coarsest grain structure at an average of 29 μm, especially the corrosion rates of this alloy remain the highest and least homogeneous of this study with more than 0.4 mm/y after 7 days. In combination with Ca, the properties could be enhanced in alloy IX10. Equiaxed microstructures with typical average grain sizes around 10 μm are obtained. All other alloys with Ca as an additional alloying element exhibit a distinct embrittlement of the wires after exposure to the corrosive environment. The binary Mg-Y alloy W0 was found to maintain a comparable property profile after corrosion exposure with the lowest loss in fracture strain, highest TYS at 201 MPa and highest UTS at 256 MPa, accompanied by homogeneous and low corrosion rate, below 0.2 mm/y in artificial urine solution.

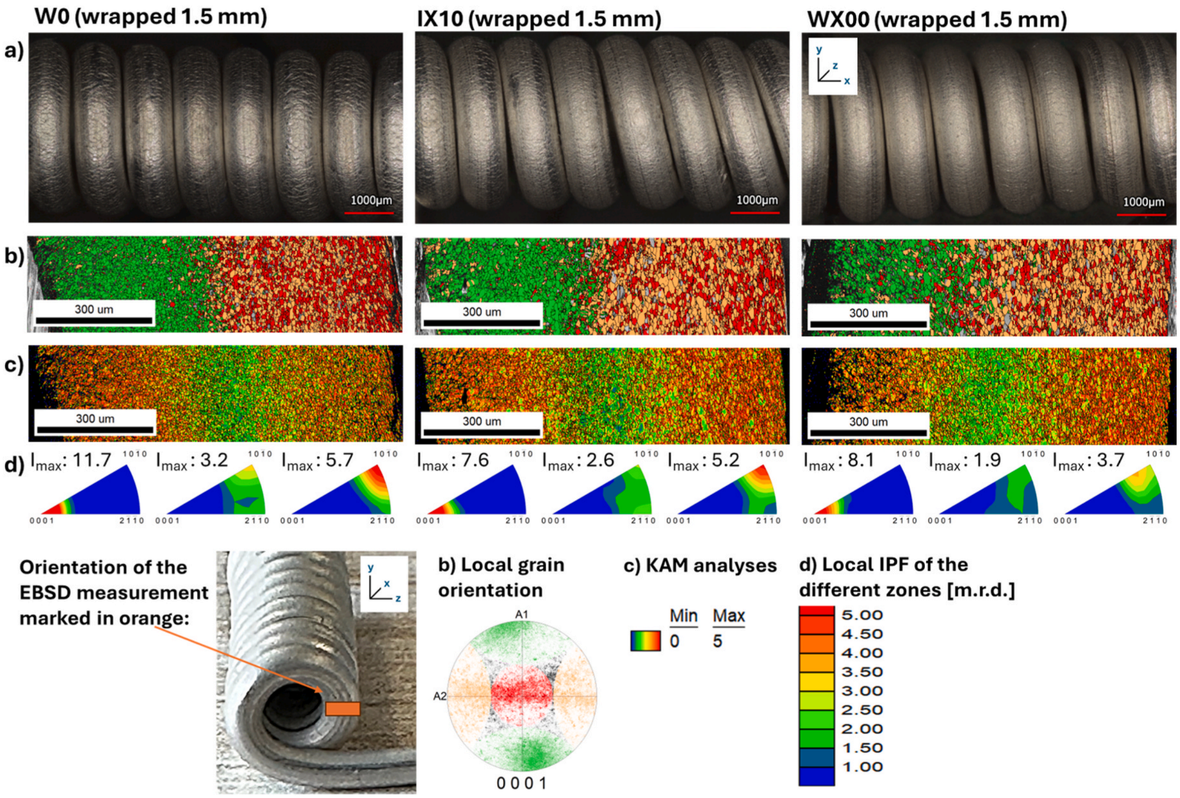

Fig. 9. a) Optical images of the wrapped wires, inner diameter = 1.5 mm; b) EBSD of cross section from a wrapped section with highlighted grain orientation as marked in the (0001) pole figure; c) with highlighted KAM analyses; d) local inverse pole figures (IPF) of the different zones.

CRediT authorship contribution statement

Maria Nienaber: Writing – review & editing, Writing – original draft, Visualization, Validation, Methodology, Investigation, Formal analysis, Data curation, Conceptualization. **Mengyao Liu:** Writing – review & editing, Visualization, Validation, Investigation, Formal analysis, Data curation. **Margarida Pacheco:** Writing – review & editing, Writing – original draft, Conceptualization. **Fabian Esterl:** Writing – review & editing, Writing – original draft, Visualization, Methodology, Investigation, Formal analysis. **Merle Braatz:** Writing – review & editing, Conceptualization. **Alexandre Barros:** Writing – review & editing, Project administration, Conceptualization. **Rui L. Reis:** Writing – review & editing. **Mikhail L. Zheludkevich:** Writing – review & editing. **Noomane Ben Khalifa:** Writing – review & editing. **Sviatlana V. Lamaka:** Writing – review & editing, Writing – original draft, Project administration, Funding acquisition, Formal analysis, Conceptualization. **Jan Bohlen:** Writing – review & editing, Writing – original draft, Project administration, Funding acquisition, Formal analysis, Conceptualization.

Declaration of competing interest

The authors declare that they have no known competing financial interests or personal relationships that could have appeared to influence the work reported in this paper.

Acknowledgement

Ms. Petra Mario Fischer of “Electrochemistry and Big-Data” of Institute of Surface Science of Hereon is acknowledged for acquiring SEM micrographs of the wires after corrosion. The authors would like to thank Mr. Günther Meister and Mr. Alexander Reichart for their help during casting and machining of the billets. Ms. Mengyao Liu acknowledges her CSC grant (No. 202207040039). The collaborative German-Portuguese DAAD-FCT project ID: 57665092 is acknowledged for the financial support.

Data availability

Data will be made available on request.

References

[1] R. Zan, W. Ji, S. Qiao, H. Wu, W. Wang, T. Ji, B. Yang, S. Zhang, C. Luo, Y. Song, J. Ni, X. Zhang, Biodegradable magnesium implants: a potential scaffold for bone tumor patients, Sci. China Mater. 64 (4) (2020) 1007–1020, https://doi.org/10.1007/s40843-020-1509-2.

[2] X. He, Y. Li, H.W. Miao, J. Sun, M.T.Y. Ong, H.Y. Zu, W.S. Li, The bioactive mg-zn-gd wire enhances musculoskeletal regeneration: an in vitro study, Crystals 12 (9) (2022), https://doi.org/10.3390/cryst12091287.

[3] D. Xia, F. Yang, Y. Zheng, Y. Liu, Y. Zhou, Research status of biodegradable metals designed for oral and maxillofacial applications: a review, Bioact. Mater. 6 (11) (2021) 4186–4208, https://doi.org/10.1016/j.bioactmat.2021.01.011.

[4] M. Pacheco, I.M. Aroso, J.M. Silva, S.V. Lamaka, J. Bohlen, M. Nienaber, D. Letzig, E. Lima, A.A. Barros, R.L. Reis, Understanding the corrosion of Mg alloys in in vitro urinary tract conditions: a step forward towards a biodegradable metallic ureteral stent, J. Magnesium Alloys 11 (11) (2023) 4301–4324, https://doi.org/10.1016/j.jma.2023.10.002.

[5] R. Biber, J. Pauser, M. Brem, H.J. Bail, Bioabsorbable metal screws in traumatology: a promising innovation, Trauma Case Rep 8 (2017) 11–15, https://doi.org/10.1016/j.tcr.2017.01.012.

[6] S. Jayasathyakawin, M. Ravichandran, R. Naveenkumar, N. Radhika, S.O. Ismail, V. Mohanavel, Recent advances in magnesium alloys for biomedical applications: a review, Mater. Today Commun. 42 (2025), https://doi.org/10.1016/j.mtcomm.2024.111239.

[7] A. Milenin, P. Kustra, D. Byrska-Wojcik, M. Wrobel, M. Packo, J. Sulej-Chojnacka, S. Matuszynska, B. Plonka, The effect of in vitro corrosion on the mechanical properties of metallic high strength biodegradable surgical threads, Arch. Civ. Mech. Eng. 20 (2) (2020), https://doi.org/10.1007/s43452-020-00062-w.

[8] J.E. Bergsma, F.R. Rozema, R.R.M. Bos, G. Boering, W.C. de Bruijn, Late degradation tissue response to poly(l-lactide) bone plates and screws, in: D. F. Williams (Ed.), The Biomaterials: Silver Jubilee Compendium, Elsevier Science, Oxford, 1995, pp. 101–107, https://doi.org/10.1016/B978-008045154-1.50014-9.

[9] J. Chen, L. Tan, X. Yu, I.P. Etim, M. Ibrahim, K. Yang, Mechanical properties of magnesium alloys for medical application: a review, J. Mech. Behav. Biomed. Mater. 87 (2018) 68–79, https://doi.org/10.1016/j.jmbbm.2018.07.022.
[10] M.H. Yoo, Slip, twinning, and fracture in hexagonal close-packed metals, Metall. Trans. A 12 (3) (1981) 409–418, https://doi.org/10.1007/Bf02648537.
[11] J. Hirsch, T. Al-Samman, Superior light metals by texture engineering: optimized aluminum and magnesium alloys for automotive applications, Acta Mater. 61 (3) (2013) 818–843, https://doi.org/10.1016/j.actamat.2012.10.044.
[12] S. Sandlobes, M. Friak, S. Korte-Kerzel, Z. Pei, J. Neugebauer, D. Raabe, A rare-earth free magnesium alloy with improved intrinsic ductility, Sci. Rep. 7 (1) (2017) 10458, https://doi.org/10.1038/s41598-017-10384-0.
[13] N.P. Papenberg, S. Gneiger, P.J. Uggowitzer, S. Pogatscher, Lean wrought magnesium alloys, Materials 14 (15) (2021), https://doi.org/10.3390/ma14154282.
[14] X. Gu, Y. Zheng, Y. Cheng, S. Zhong, T. Xi, In vitro corrosion and biocompatibility of binary magnesium alloys, Biomaterials 30 (4) (2009) 484–498, https://doi.org/10.1016/j.biomaterials.2008.10.021.
[15] N. Stanford, Micro-alloying Mg with Y, Ce, Gd and La for texture modification-a comparative study, Mater. Sci. Eng. (2010), https://doi.org/10.1016/j.msea.2009.12.036.
[16] A.G. Beer, 8 - enhancing the extrudability of wrought magnesium alloys, in: C. Bettles, M. Barnett (Eds.), Advances in Wrought Magnesium Alloys, Woodhead Publishing, 2012, pp. 304–322, https://doi.org/10.1533/9780857093844.2.304.
[17] D. Mei, C. Wang, M. Nienaber, M. Pacheco, A. Barros, S. Neves, R.L. Reis, S.J. Zhu, J. Bohlen, D. Letzig, S.K. Guan, M.L. Zheludkevich, S.V. Lamaka, Corrosion behavior of Mg wires for ureteral stent in artificial urine solution, Corros. Sci. 189 (2021), https://doi.org/10.1016/j.corsci.2021.109567.
[18] Y. Zhang, J. Cao, M. Lu, Y. Shao, K. Jiang, X. Yang, X. Xiong, S. Wang, C. Chu, F. Xue, Y. Ye, J. Bai, A biodegradable magnesium surgical staple for colonic anastomosis: in vitro and in vivo evaluation, Bioact. Mater. 22 (2023) 225–238, https://doi.org/10.1016/j.bioactmat.2022.09.023.
[19] Z. Mardina, J. Venezuela, T. Sjafrizal, Z.M. Shi, M.S. Dargusch, A. Atrens, The influence of strain rate and annealing heat treatments on the corrosion and mechanical properties of WE43 and Zn7Ag biodegradable wires for application in soft tissue reconstructions, Mater. Today Commun. 35 (2023), https://doi.org/10.1016/j.mtcomm.2023.105809.
[20] Z.Q. Gao, X.Y. Zhang, H. Huang, C. Chen, J.M. Jiang, J.L. Niu, M. Dargusch, G. Y. Yuan, Microstructure evolution, mechanical properties and corrosion behavior of biodegradable Zn-2Cu-0.8Li alloy during room temperature drawing, Mater. Char. 185 (2022), https://doi.org/10.1016/j.matchar.2022.111722.
[21] A. Milenin, M. Wróbel, P. Kustra, M. Packo, D. Byrska-Wójcik, J. Sulej-Chojnacka, B. Płonka, Mechanical properties, crystallographic texture, and in vitro bio-corrosion of low-alloyed Zn–Mg, produced by hot and cold drawing for biodegradable surgical wires, Arch. Civ. Mech. Eng. 21 (4) (2021), https://doi.org/10.1007/s43452-021-00311-6.
[22] U. Reddy, D. Dubey, S.S. Panda, N. Ireddy, J. Jain, K. Mondal, S.S. Singh, Effect of surface roughness induced by milling operation on the corrosion behavior of magnesium alloys, J. Mater. Eng. Perform. 30 (10) (2021) 7354–7364, https://doi.org/10.1007/s11665-021-05933-8.
[23] P. Zhang, Y. Huang, R. Wang, K. Ohashi, Study of machined surface quality of AZ31B magnesium alloy by end milling, Metals 13 (2023) 1712, https://doi.org/10.3390/met13101712.
[24] M. Yin, L. Hou, Z. Wang, T. Bao, B. Liu, H. Wei, X. Liu, H. Du, Y. Wei, Self-generating construction of applicable corrosion-resistant surface structure of magnesium alloy, Corros. Sci. 184 (2021), https://doi.org/10.1016/j.corsci.2021.109378.
[25] J. Kubasek, D. Vojtech, J. Lipov, T. Ruml, Structure, mechanical properties, corrosion behavior and cytotoxicity of biodegradable Mg-X (X=Sn, Ga, in) alloys, Mater. Sci. Eng., C 33 (4) (2013) 2421–2432, https://doi.org/10.1016/j.msec.2013.02.005.
[26] M. Deng, D. Höche, S.V. Lamaka, D. Snihirova, M.L. Zheludkevich, Mg-Ca binary alloys as anodes for primary Mg-air batteries, J. Power Sources 396 (2018) 109–118, https://doi.org/10.1016/j.jpowsour.2018.05.090.
[27] M. Deng, L. Wang, D. Snihirova, J. Bohlen, G. Kurz, S.V. Lamaka, D. Höche, M. L. Zheludkevich, Micro-alloyed Mg-Ca: corrosion susceptibility to heating history and a plain problem-solving approach, J. Magnesium Alloys 11 (4) (2023) 1193–1205, https://doi.org/10.1016/j.jma.2022.12.014.
[28] L. Berger, S. Dolert, T. Akhmetshina, J.P. Burkhard, M. Tegelkamp, A.M. Rich, W. Rubin, S. Darwiche, G. Kuhn, R.E. Schaublin, B. von Rechenberg, B. Schaller, K. M. Nuss, J.F. Loffler, In vivo performance of lean bioabsorbable Mg-Ca alloy X0 and comparison to WE43: influence of surface modification and alloying content, Bioact. Mater. 44 (2025) 501–515, https://doi.org/10.1016/j.bioactmat.2024.09.036.
[29] X. Liu, D. Shan, Y. Song, E.-h. Han, Influence of yttrium element on the corrosion behaviors of Mg–Y binary magnesium alloy, J. Magnesium Alloys 5 (1) (2017) 26–34, https://doi.org/10.1016/j.jma.2016.12.002.
[30] W. Ci, L. Deng, X. Chen, C. Liu, F. Pan, Effect of minor Ca addition on microstructure and corrosion behavior of mg–y–ca alloys, J. Mater. Res. Technol. 26 (2023) 7502–7515, https://doi.org/10.1016/j.jmrt.2023.09.112.
[31] M. Nienaber, J. Bohlen, G. Kurz, D. Letzig, Deciphering the effects of rolling temperature on the texture development and formability of W1 and WZ10 Magnesium alloy, J. Alloys Compd. (2024), https://doi.org/10.1016/j.jallcom.2024.177783.
[32] W. Tang, G. Zhou, Y. Shao, D. Li, Y. Peng, H. Wang, On the role of yttrium in microstructure evolution and texture modification during magnesium alloy extrusion, Mater. Char. 162 (2020), https://doi.org/10.1016/j.matchar.2020.110189.
[33] N. Ansari, R. Sarvesha, S.Y. Lee, S.S. Singh, J. Jain, Influence of yttrium addition on recrystallization, texture and mechanical properties of binary Mg-Y alloys, Mater. Sci. Eng. 793 (2020) 139856, https://doi.org/10.1016/j.msea.2020.139856.
[34] F. Mouhib, Z. Xie, A. Atila, J. Guénolé, S. Korte-Kerzel, T. Al-Samman, Exploring solute behavior and texture selection in magnesium alloys at the atomistic level, Acta Mater. 266 (2024), https://doi.org/10.1016/j.actamat.2024.119677.
[35] J.-Y. Lee, Y.-S. Yun, B.-C. Suh, N.-J. Kim, W.-T. Kim, D.-H. Kim, Comparison of static recrystallization behavior in hot rolled Mg–3Al–1Zn and Mg–3Zn–0.5Ca sheets, J. Alloys Compd. 589 (2014) 240–246, https://doi.org/10.1016/j.jallcom.2013.11.210.
[36] Z. Ling, M. Chen, L. Wang, K. Ma, D. Zhang, Y. Li, Z. Zhang, Z. Zhao, P. Bai, Y. Li, Microstructure evolution and mechanical property of Mg-Gd-Y-Zn-Zr alloy wires prepared by hot drawing, J. Mater. Res. Technol. 30 (2024) 782–793, https://doi.org/10.1016/j.jmrt.2024.03.140.
[37] M. Gao, I.P. Etim, K. Yang, L. Tan, Z. Ma, Enhancing mechanical property and corrosion resistance of Mg–Zn-Nd alloy wire by a combination of SPD techniques, extrusion and hot drawing, Mater. Sci. Eng. 829 (2022), https://doi.org/10.1016/j.msea.2021.142058.
[38] M. Nienaber, S.B. Yi, K.U. Kainer, D. Letzig, J. Bohlen, On the direct extrusion of magnesium wires from mg-al-zn series alloys, Metals 10 (9) (2020) 1208, https://doi.org/10.3390/met10091208.
[39] A. Jager, S. Habr, K. Tesar, Twinning-detwinning assisted reversible plasticity in thin magnesium wires prepared by one-step direct extrusion, Mater. Des. 110 (2016) 895–902, https://doi.org/10.1016/j.matdes.2016.08.016.
[40] K. Tesar, K. Balik, Z. Sucharda, A. Jager, Direct extrusion of thin Mg wires for biomedical applications, Trans. Nonferrous Met. Soc. China 30 (2) (2020) 373–381, https://doi.org/10.1016/S1003-6326(20)65219-0.
[41] N. Sarigul, F. Korkmaz, I. Kurultak, A new artificial urine protocol to better imitate human urine, Sci. Rep. 9 (1) (2019) 20159, https://doi.org/10.1038/s41598-019-56693-4.
[42] D. Mei, S.V. Lamaka, C. Feiler, M.L. Zheludkevich, The effect of small-molecule bio-relevant organic components at low concentration on the corrosion of commercially pure Mg and Mg-0.8Ca alloy: an overall perspective, Corros. Sci. 153 (2019) 258–271, https://doi.org/10.1016/j.corsci.2019.03.039.
[43] J. Nachtsheim, J. Burja, S. Ma, B. Markert, Long-term in vitro corrosion of biodegradable WE43 magnesium alloy in DMEM, Metals 12 (12) (2022), https://doi.org/10.3390/met12122062.
[44] D. Mei, Q. Zhang, Y. Li, M. Liu, W. Li, P. Jiang, R. Hou, S. Zhu, L. Wang, S. Guan, The misalignment between degradation rate and mechanical integrity of Mg-Zn-Y-Nd alloy during the degradation evaluation in modified Hanks' solutions, J. Magnesium Alloys 12 (9) (2024) 3661–3674, https://doi.org/10.1016/j.jma.2023.04.006.
[45] Q. Xie, A. Ma, J. Jiang, H. Liu, Z. Cheng, Y. Gu, Tailoring the corrosion behavior and mechanism of AZ31 magnesium alloys by different Ca contents for marine application, Corros. Sci. 192 (2021), https://doi.org/10.1016/j.corsci.2021.109842.
[46] F. Esterl, M. Nienaber, J. Bohlen, N. Ben Khalifa, Connecting texture development to die design in extruded flat products, J. Manuf. Process. 134 (2025) 891–903, https://doi.org/10.1016/j.jmapro.2024.12.078.
[47] A.N. Levanov, Improvement of metal forming processes by means of useful effects of plastic friction, J. Mater. Process. Technol. 72 (1997) 314–316, https://doi.org/10.1016/S0924-0136(97)00191-X.
[48] M. Nienaber, M. Braatz, N. Ben Khalifa, J. Bohlen, Property profile development during wire extrusion and wire drawing of magnesium alloys AZ31 and ZX10, Mater. Des. 224 (2022), https://doi.org/10.1016/j.matdes.2022.111355.
[49] S.M. Zhu, J.F. Nie, M.A. Gibson, M.A. Eastona, On the unexpected formation of rare earth hydrides in magnesium-rare earth casting alloys, Scr. Mater. 77 (2014) 21–24, https://doi.org/10.1016/j.scriptamat.2014.01.007.
[50] J.F. Nie, K.S. Shin, Z.R. Zeng, Microstructure, deformation, and property of Wrought magnesium alloys, Metall. Mater. Trans. A 51 (12) (2020) 6045–6109, https://doi.org/10.1007/s11661-020-05974-z.
[51] M.G. Jiang, C. Xu, H. Yan, G.H. Fan, T. Nakata, C.S. Lao, R.S. Chen, S. Kamado, E. H. Han, B.H. Lu, Unveiling the formation of basal texture variations based on twinning and dynamic recrystallization in AZ31 magnesium alloy during extrusion, Acta Mater. 157 (2018) 53–71, https://doi.org/10.1016/j.actamat.2018.07.014.
[52] N. Stanford, M.R. Barnett, The origin of "rare earth" texture development in extruded Mg-based alloys and its effect on tensile ductility, Mater. Sci. Eng. 496 (1-2) (2008) 399–408, https://doi.org/10.1016/j.msea.2008.05.045.
[53] M.G. Jiang, C. Xu, H. Yan, S.H. Lu, T. Nakata, C.S. Lao, R.S. Chen, S. Kamado, E. H. Han, Correlation between dynamic recrystallization and formation of rare earth texture in a mg-zn-gd magnesium alloy during extrusion, Sci. Rep. 8 (1) (2018) 16800, https://doi.org/10.1038/s41598-018-35170-4.
[54] I. Basu, T. Al-Samman, Triggering rare earth texture modification in magnesium alloys by addition of zinc and zirconium, Acta Mater. 67 (2014) 116–133, https://doi.org/10.1016/j.actamat.2013.12.015.
[55] G. Cano-Castillo, J. Victoria-Hernandez, J. Bohlen, D. Letzig, K.U. Kainer, Effect of Ca and Nd on the microstructural development during dynamic and static recrystallization of indirectly extruded Mg-Zn based alloys, Mater. Sci. Eng. 793 (2020), https://doi.org/10.1016/j.msea.2020.139527.
[56] A. International, Standard Specification for Ureteral Stents, F, ASTM standard, 2006, pp. 1828–1897, in *with AUS composition*.
[57] C. Wang, C. Tonna, D. Mei, J. Buhagiar, M.L. Zheludkevich, S.V. Lamaka, Biodegradation behaviour of Fe-based alloys in Hanks' Balanced Salt Solutions: part II. The evolution of local pH and dissolved oxygen concentration at metal

interface, Bioact. Mater. 7 (2022) 412–425, https://doi.org/10.1016/j.bioactmat.2021.05.014.

[58] C. Wang, X. Liu, D. Mei, M. Deng, Y. Zheng, M.L. Zheludkevich, S.V. Lamaka, Local pH and oxygen concentration at the interface of Zn alloys in Tris-HCl or HEPES buffered Hanks' balanced salt solution, Corros. Sci. (2022) 110061, https://doi.org/10.1016/j.corsci.2021.110061.

[59] C. Wang, K. Qian, Y. Wu, D. Mei, C. Chu, F. Xue, J. Bai, M.L. Zheludkevich, S. V. Lamaka, Consistent high rate oxygen reduction reaction during corrosion of Mg-Ag alloy, Corros. Sci. (2024) 111893, https://doi.org/10.1016/j.corsci.2024.111893.

[60] C. Wang, D. Mei, G. Wiese, L.Q. Wang, M. Deng, S.V. Lamaka, M.L. Zheludkevich, High rate oxygen reduction reaction during corrosion of ultra-high-purity magnesium, npj Mater. Degrad. 4 (1) (2020) 42, https://doi.org/10.1038/s41529-020-00146-1.

[61] D. Tie, H. Liu, R. Guan, P. Holt-Torres, Y. Liu, Y. Wang, N. Hort, In vivo assessment of biodegradable magnesium alloy ureteral stents in a pig model, Acta Biomater. 116 (2020) 415–425, https://doi.org/10.1016/j.actbio.2020.09.023.

[62] B.H. Chew, D. Lange, Ureteral stent symptoms and associated infections: a biomaterials perspective, Nat. Rev. Urol. 6 (8) (2009) 440–448, https://doi.org/10.1038/nrurol.2009.124.

[63] X.H. Zhou, C.W. Ha, S.B. Yi, J. Bohlen, N. Schell, Y.Q. Chi, M.Y. Zheng, H. G. Brokmeier, Texture and lattice strain evolution during tensile loading of Mg-Zn alloys measured by synchrotron diffraction, Metals 10 (1) (2020), https://doi.org/10.3390/met10010124.

[64] N.V. Dudamell, I. Ulacia, F. Galvez, S. Yi, J. Bohlen, D. Letzig, I. Hurtado, M. T. Perez-Prado, Twinning and grain subdivision during dynamic deformation of a Mg AZ31 sheet alloy at room temperature, Acta Mater. 59 (18) (2011) 6949–6962, https://doi.org/10.1016/j.actamat.2011.07.047.